Liquid-Gas Transition Studied via Gibbs Ensemble Monte Carlo Simulations

Juan Manuel Henning

Abstract

The main idea of the project is to investigate the liquid-gas transition of a fore-shifted Lenard-Jones particle system via Gibbs ensemble Monte Carlo simulations. In particular, we wish to determine the system's liquid-gas binodal in the temperature-density plane and the phase diagram in the pressure-temperature plane. We will compare the obtained binodal with results from the literature [1, 2], and we will discuss the behavior around the critical point in light of the van der Waals equation of state.

1 Introduction

The Gibbs ensemble effectively models a particle system where the chemical potential μ, pressure p, and temperature T become constant at equilibrium.

The global system, initially described by the (N, V, T) canonical ensemble, is split into subsystems I and II, with

$$N = N_{\mathrm{I}} + N_{\mathrm{II}}, \quad V = V_{\mathrm{I}} + V_{\mathrm{II}}, \quad T = T_{\mathrm{I}} = T_{\mathrm{II}}. \quad (1)$$

Particles in subsystem I do not interact with particles in subsystem II. The subsystems equilibrate with respect to each other via the Gibbs ensemble Monte Carlo simulation (GEMCS).

2 Interaction Potential

The interaction potential describes the particle-particle interaction, i.e., the interaction between two particles separated by a distance r. The Lenard-Jones potential models the particle-particle interaction by the function

$$\phi(r)_{\alpha\gamma} = \begin{cases} 4\epsilon\left[\left(\frac{\sigma}{r}\right)^{12} - \left(\frac{\sigma}{r}\right)^{6}\right]\delta_{\alpha\gamma} = & , \quad r \le r_c, \\ 0 & , \quad r > r_c. \end{cases} \quad (2)$$

Here, the additional $\delta_{\alpha\gamma}$ factor, with subsystem indices $\alpha, \gamma \in \{\mathrm{I}, \mathrm{II}\}$, accounts for the absence of interaction between particles of different subsystems. We will focus on the interaction potential given by the force-shifted Lennard-Jones (fsLJ) potential

$$U(r) \equiv U_{fsLJ}(r) = \phi(r) - \phi(r_c) - (r - r_c) \left.\frac{\mathrm{d}\phi(r)}{\mathrm{d}r}\right|_{r=r_c}, \quad (3)$$

with the cutoff parameter set to $r_c = 2.5\,\sigma$. Note that the subsystem's indices, α and γ, are omitted for simplicity. We will use reduced units for quantities that involve energy and length, effectively setting their characteristic parameters to $k_B = \epsilon = \sigma = 1$.
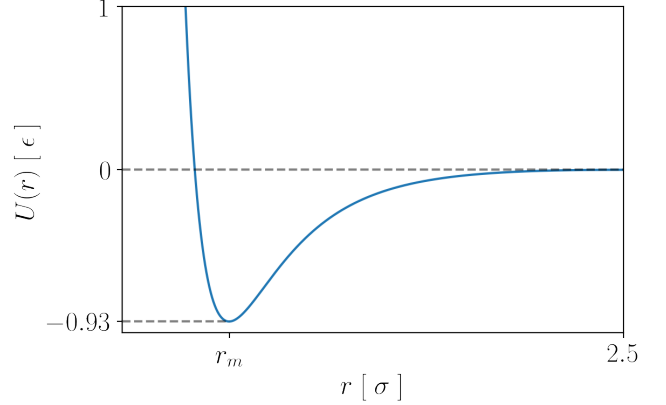

Figure 1: The force-shifted Lennard-Jones potential is plotted in units of ϵ, as a function of the particle-particle distance in units of σ. The potential minimum in reduced units is given by $U(r_m) \approx -0.93$, with $r_m \approx 1.123$.

3 Gibbs Ensemble MC Simulation

The GEMCS aims to form an effective "(μ, p, T) ensemble", i.e., $\mu_{\mathrm{I}} = \mu_{\mathrm{II}}$, $p_{\mathrm{I}} = p_{\mathrm{II}}$, $T_{\mathrm{I}} = T_{\mathrm{II}}$ at equilibrium. Note that the total system is always in a canonical (N, V, T) ensemble. The simulation consists of many Monte Carlo (MC) steps, at which, one of three types of MC moves is randomly chosen.

MC move	Probability	Ensemble
Particle Displacement	P_d	$(N, V, T)_\alpha$
Particle Exchange	P_n	$(\mu, V, T)_\alpha$
Volume Exchange	P_v	$(N, p, T)_\alpha$

Table 1: One MC move is randomly chosen at every step of the GEMCS with its respective probability, following the normalization condition $P_d + P_n + P_v = 1$. The three different MC moves used in the GEMCS correspond to different ensembles of subsystem $\alpha \in \{\mathrm{I}, \mathrm{II}\}$.

The length of the simulation is given in terms of MC steps and MC sweeps, with

$$\#\text{MC sweeps} = \frac{\#\text{MC steps}}{N}. \quad (4)$$

We will now take a closer look at the different types of MC moves mentioned in Table 1, in the context of a 3D particle system with cubic subsystems, i.e., $V_\alpha = l_\alpha{}^3$ for $\alpha \in \{\mathrm{I}, \mathrm{II}\}$. We will refer to uniform random variables as "random" variables, for simplicity.

3.1 Particle Displacement

One of the subsystems, $\alpha \in \{I,II\}$, is chosen at random. A particle of the chosen subsystem is randomly selected, and displaced in a random direction, given by

$$\vec{r}_{\alpha,\text{old}} \to \vec{r}_{\alpha,\text{new}} = \vec{r}_{\alpha,\text{old}} + d\vec{r}, \qquad (5)$$

with random displacement components $dx, dy, dz \in [-d_{\max}, d_{\max}]$. The Metropolis criterion, i.e., the displacement acceptance-probability is given by

$$P_{\text{acc}}^d(\text{old} \to \text{new}) = \min\left(1, e^{-\beta\left(U\left(\vec{R}_{\alpha,\text{new}}\right) - U\left(\vec{R}_{\alpha,\text{old}}\right)\right)}\right), \ (6)$$

where $\beta = 1/T$ in reduced units, and $\vec{R}_\alpha = (\vec{r}_1, \vec{r}_2, \ldots, \vec{r}_{N_\alpha})$ represents the position of the N_α particles in subsystem α. The term $U(\vec{R}_\alpha)$, given by

$$U(\vec{R}_\alpha) = \sum_{i=1}^{N_\alpha} \sum_{\substack{j=1 \\ j>i}}^{N_\alpha} U(r_{ij}), \quad \text{with } r_{ij} = |\vec{r}_i - \vec{r}_j|, \quad (7)$$

represents the total potential energy of subsystem α. We use labels "old" and "new" for particle configurations before and after displacement.

3.2 Particle Exchange

A particle is chosen in the same way as in the *Particle Displacement* MC move and transferred to a random position in the other subsystem. The change in particle number is given by

$$\begin{aligned} N_{\alpha,\text{old}} &\to N_{\alpha,\text{new}} = N_{\alpha,\text{old}} - 1, \\ N_{\gamma,\text{old}} &\to N_{\gamma,\text{new}} = N_{\gamma,\text{old}} + 1, \end{aligned} \quad (8)$$

with $\gamma \neq \alpha$, and an acceptance-probability of

$$\begin{aligned} P_{\text{acc}}^n(\text{old} &\to \text{new}) = \\ &\min\left(1, \frac{N_\alpha}{N_\gamma + 1} \frac{V_\gamma}{V_\alpha} e^{-\beta\left(U\left(\vec{R}_{\text{new}}\right) - U\left(\vec{R}_{\text{old}}\right)\right)}\right), \end{aligned} \quad (9)$$

with $U(\vec{R}) = U(\vec{R}_I) + U(\vec{R}_{II})$ for "old" and "new" configurations respectively.

3.3 Volume Exchange

Volume can be exchanged between the two subsystems. As before, $\alpha \in \{I, II\}$ is chosen at random. The change in volume is given by

$$\begin{aligned} V_{\alpha,\text{old}} &\to V_{\alpha,\text{new}} = V_{\alpha,\text{old}} + dV, \\ V_{\gamma,\text{old}} &\to V_{\gamma,\text{new}} = V_{\gamma,\text{old}} - dV, \end{aligned} \quad (10)$$

with $\alpha \neq \gamma$, and $dV \in [-dV_{\max}, dV_{\max}]$. Note that the change of volume in both subsystems is performed isotropically. Therefore, the position of the particles in the new volumes has to be scaled accordingly. The new particle coordinates for subsystem α (analogously for subsystem γ) are given by the transformation

$$\vec{r}_{\alpha,\text{old}} \to \vec{r}_{\alpha,\text{new}} = \frac{l_{\alpha,\text{new}}}{l_{\alpha,\text{old}}} \vec{r}_{\alpha,\text{old}}, \qquad (11)$$

with $l_\alpha = V_\alpha^{1/3}$ for "old" and "new" volumes respectively. The volume-exchange acceptance-probability is given by

$$P_{\text{acc}}^v(\text{old} \to \text{new}) =$$
$$\min\left(1, \left(\frac{V_{\alpha,\text{new}}}{V_{\alpha,\text{old}}}\right)^{N_\alpha} \left(\frac{V_{\gamma,\text{new}}}{V_{\gamma,\text{old}}}\right)^{N_\gamma} e^{-\beta\left(U\left(\vec{R}_{\text{new}}\right) - U\left(\vec{R}_{\text{old}}\right)\right)}\right).$$
$$(12)$$

Note, that computing $U(\vec{R}_{\text{new}})$ from scratch should be avoided, as it is computationally expensive (see Appendix A).

4 Simulation Results

The thermodynamic variables of the global (N, V, T) system are set to $N = 750$, and $V = 1500$, in reduced units. The two 3D particle sytems, i.e., subsystems I and II, are initialized with $N_I = N_{II} = N/2$, and $V_I = V_{II} = V/2$, in random configurations.

The displacement and volume-exchange parameters are set to $d_{\max} = 0.05$, and $dV_{\max} = 100$, as they were shown to provided good equilibrium convergence.

Simulations are run for $T \in \{0.7, 0.725, 0.75, 0.775, 0.8, 0.825, 0.85, 0.875\}$.

4.1 Thermal Equilibrium

First, each subsystem reaches thermal equilibrium by doing $2 \cdot 10^3$ MC sweeps of displacement MC moves.
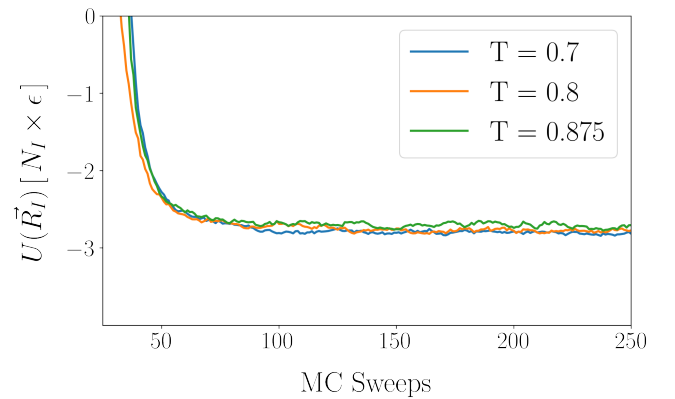

Figure 2: The average potential energy per particle of subsystem I is plotted as a function of the displacement MC sweeps. Thermal equilibrium is reached after approximately 125 MC sweeps for all temperatures of the GEMCS. Here, thermalization for $T = 0.7$ (blue), $T = 0.8$ (orange), and $T = 0.875$ (green) are shown; color online.

The average potential energy in Fig. 2 reaches a constant average value after approximately 150 MC sweeps, which means that thermal equilibrium has been reached. We then compute the radial distribution function of subsystem I, $g(r)$, to check for a typical fluid "structure".
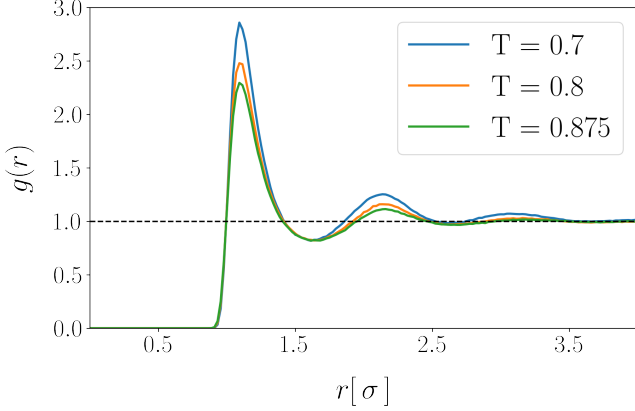

Figure 3: The radial distribution function is given by the average particle density at distance r from a given particle, normalized by the average particle density for an ideal gas. The graphs shown for $T = 0.7$ (blue), $T = 0.8$ (orange), and $T = 0.875$ (green) are typical for a fluid (see lecture notes [3]); color online.

From Figs. 3 and 2 we conclude that the subsystems are in the state of a typical fluid at thermal equilibrium, and we continue with the simulation, as described in Section 3.

4.2 Gibbs Ensemble Equilibrium

The MC moves' probabilities (see Table 1) are set to $P_d = \frac{1000}{1101}$, $P_n = \frac{100}{1101}$, and $P_v = \frac{1}{1101}$, as they provided good equilibrium convergence. Both subsystems equilibrate with respect to each other over a total simulation length of 10^5 MC sweeps. Note, that an increased simulation length of $2 \cdot 10^5$ MC sweeps was used for $T = 0.875$. The parameter $dV_{\max}$ was also changed to 10 for that particular temperature.

Figure 4 shows the convergence of the subsystems' total potential energy U_α, particle number N_α, and volume V_α towards an equilibrium value. The equilibrium point, i.e., the point after which all previously mentioned variables have equilibrated, is reached after approximately $5 \cdot 10^4$ MC sweeps (see dashed lines in Fig. 4). We compute the equilibrium averages of the thermodynamic quantities from this point forward, i.e., $\langle U_\alpha \rangle = U_{\mathrm{eq},\alpha}$, $\langle V_\alpha \rangle = V_{\mathrm{eq},\alpha}$, $\langle N_\alpha \rangle = N_{\mathrm{eq},\alpha}$. In addition, we see the equilibrated values for each subsystem's particle number density $\rho_{\mathrm{eq,I}}$ and $\rho_{\mathrm{eq,II}}$ (see the lower right plot in Fig. 4), which we will later use to plot the binodal in the T-ρ plane.

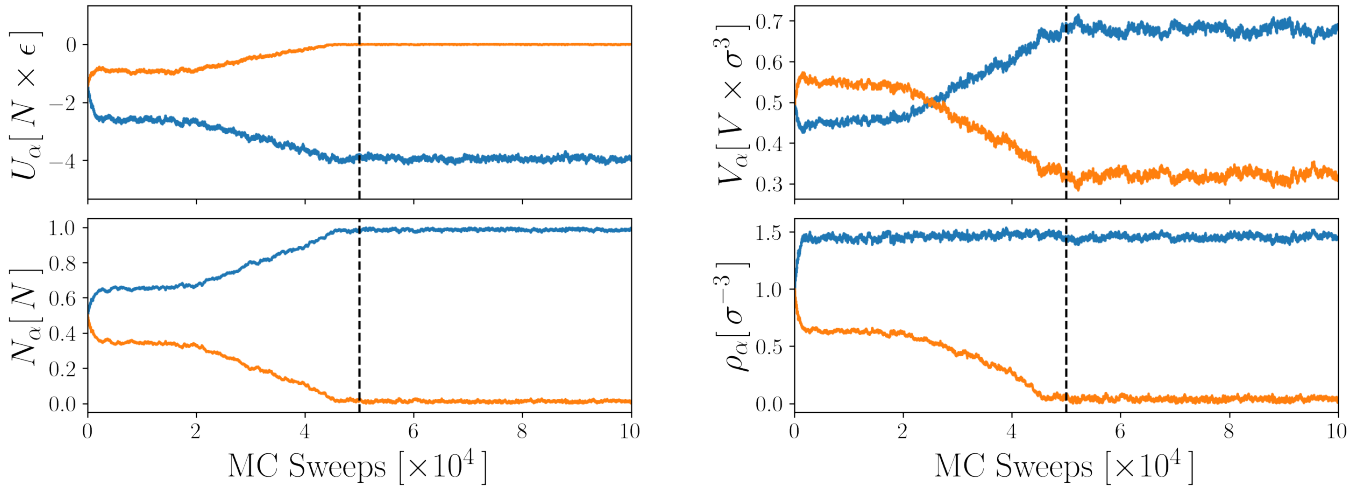

Figure 4: The equilibration of the three relevant thermodynamic variables of the two subsystems, $\alpha = $ I (orange), and $\alpha = $ II (blue), is shown exemplarily for the tamperature $T = 0.7$ (color online). The total particle number and volume are set to $N = 750$, and $V = 1500$, as previously mentioned at the beginning of Section 4. The evolution of each subsystem's potential energy U_α, volume V_α, particle number N_α, and particle density ρ_α are shown in the figure's upper left, upper right, lower left, and lower right corner respectively. The GEMCS runs over a total of 10^5 MC sweeps. The equilibrium point, i.e., the point after which equilibrium is reached in all variables, is at approximately $5 \cdot 10^4$ MC sweeps (vertical dashed line) for this particular temperature. Statistical data is collected from that point forward.
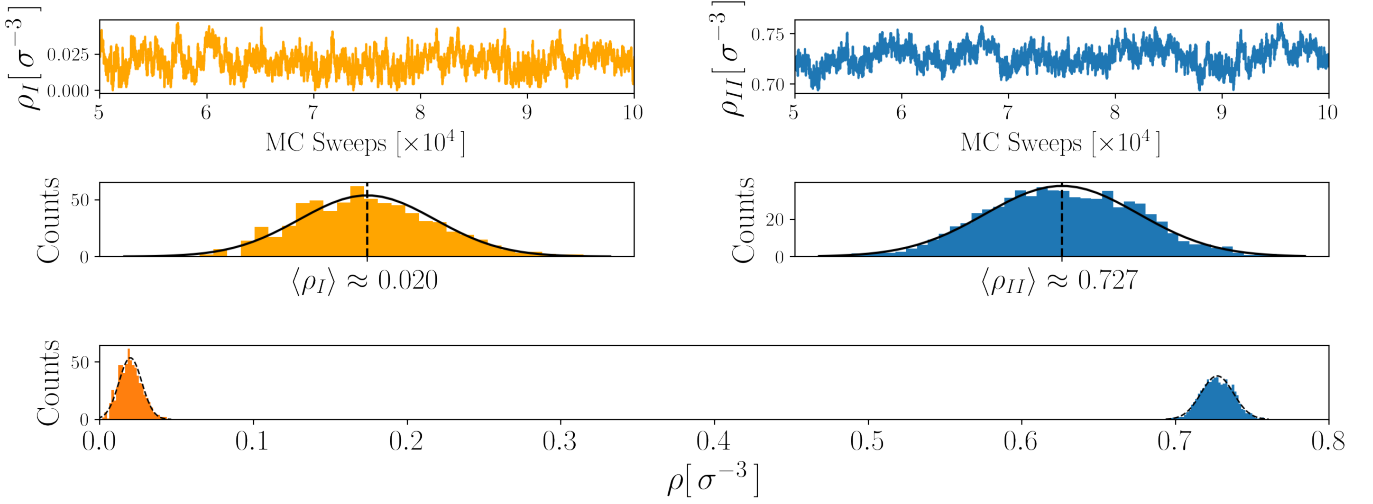
Figure 5: Data is collected from the equilibrium point forward, see Fig. 4. The fluctuation data of the subsystems' densities, ρ_I (orange), and ρ_{II} (blue), at equilibrium is shown for the temperature $T = 0.7$ (color online). The raw data from the equilibrium point forward is shown for the two subsystems (first row); a normalized histogram of the raw data is fitted with a gaussian distribution, where the mean values are marked by the dashed lines (second row); and the two data distributions are plotted together (third row). The last row mainly provides a qualitative comparison of the distributions' standard deviation (see Appendix E).

The subsystems' densities at equilibrium are determined by computing the average of the fluctuations as shown in Fig. 5. Figure 6 shows the plot of the system's T-ρ Binodal, i.e., the subsystems' densities at equilibrium for different temperatures in the T-ρ plane. Refer to Appendix B for details on the Binodal's construction, fit, and critical point estimation.
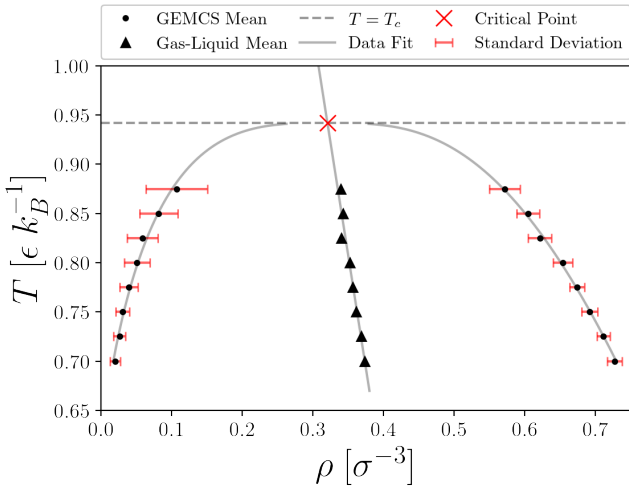

Figure 6: The system's gas (lower densities) - liquid (higher densities) binodal is plotted on the T-ρ plane, in reduced units. The dots show the results of Gibbs MC numerical simulations for different temperatures; the triangles show the average density; the gray solid line shows the data fit (see Appendix B), and a dashed line is drawn at the critical temperature $T_c \approx 0.94$. The dashed line intersects the binodal at $\rho_c \approx 0.32$ (red x). In addition, the density's standard deviation for each numerical result is plotted as a red bar; (color online). The statistical error is too small to be shown in this plot, as each dot is the result of at least $3 \cdot 10^4$ statistical data points.

The gas phase in Fig. 6 shows the largest standard deviations, i.e., fluctuations, for larger temperatures. Simulations for temperatures above $T = 0.875$ did not show any phase separation in the simulation length of 10^5 MC sweeps. The critical point on the T-ρ plane $(T_c, \rho_c) \approx (0.94, 0.32)$ can be read out from Fig. 6. We now consider the system's phase diagram in the p-T plane. The pressure of subsystem α is given by

$$p_{eq,\alpha} = \frac{1}{V_\alpha} \left[N_\alpha T + \frac{1}{3} \sum_{i=1}^{N_\alpha} \sum_{\substack{j=1 \\ j>i}}^{N_\alpha} r_{ij} \cdot \left. \frac{\partial U(r)}{\partial r} \right|_{r=r_{ij}} \right], \tag{13}$$

in reduced units. With $U(r)$ and r_{ij} as defined previously in Eqs. (3) and (7) respectively.

Analogous to the other thermodynamic variables at the beginning of this section, we write $\langle p_\alpha \rangle = p_{eq,\alpha}$ as the average value for the equilibrated pressure of subsystem α. The average pressure of both subsystems should be the same at equilibrium, i.e., $p_{eq} = p_{eq,I} = p_{eq,II}$. However, the simulation's results are not the same, due to statistical errors. Consequently, we make the approximation $p_{eq} = \frac{1}{2}(p_{eq,I} + p_{eq,II})$. The pressure at equilibrium is calculated for different temperatures and plotted in the p-T plane, see Fig. 7.

The critical point on the p-T plane $(p_c, T_c) \approx (0.10, 0.94)$ can be read out from Fig. 7. The exponential fit is given by

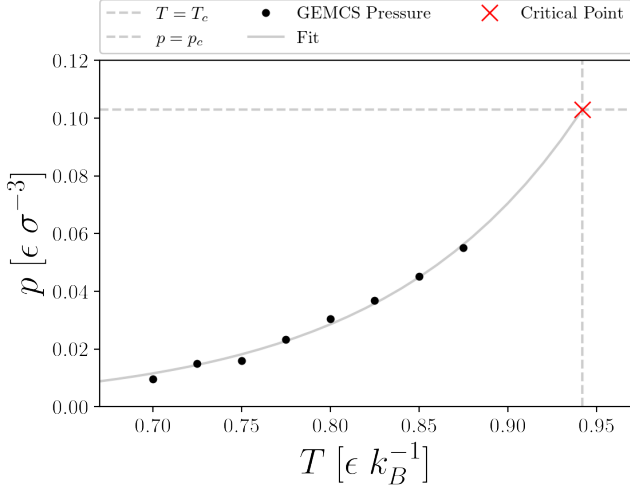$$p_{fit} \approx 2.08 \cdot 10^{-5} \, e^{9.03 \cdot T}. \tag{14}$$

Figure 7: The numerical values for the pressure at equilibrium are plotted in the p-T plane. The dots show the computed pressure at equilibrium using Eq. (13) from the Gibbs MC equilibrated numerical data. The data's exponential fit (solid gray line) intersects the critical temperature line (vertical dashed line) at the critical pressure $p_c \approx 0.10$ (horizontal dashed line). The critical point is represented by a red x.

5 Discussion

5.1 Comparison with Literature

We compare the resulting binodal, based on the force-shifted Lennard-Jones (fsLJ) potential, to the one obtained by Hansen and Verlet via MC simulations, based on a truncated Lennard-Jones potential (LJ) [1], and the one obtained by Vrabec et al. via molecular dynamics simulations, based on a truncated and shifted Lennard-Jones potential (sLJ) [2].
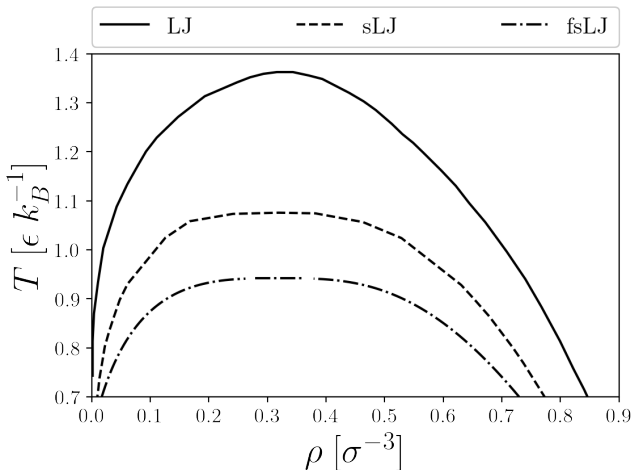

Figure 8: The gas-liquid binodal is shown for different potentials. The models were based on the LJ potential (solid line), the sLJ potential (dashed line), and the fsLJ potential (dashed-dotted line); extracted with an online digitizer tool [4]. The last one is the binodal mentioned in Fig. 6. The estimated critical temperatures depend on the chosen potential, with $T_{c,\text{LJ}} \approx 1.3$, $T_{c,\text{sLJ}} \approx 1.1$, and $T_{c,\text{fsLJ}} \approx 0.9$.

Note that the underlying potentials are all different. Hansen and Verlet consider a Lennard-Jones potential $U(r)_{\text{LJ}} = \phi(r)$; Vrabec et al. consider the pontential $U(r)_{\text{sLJ}} = \phi(r) - \phi(r_c)$, with $\phi(r)$ as defined in Eq. (2); while we consider a fsLJ potential, as defined in Eq. (3). It is not surprising, that the binodals of Fig. 8 do not match, as different potentials were used.

One way to test the dependence of T_c on the system's underlying potential would be to consider the potential

$$U_\lambda(r) = \phi(r) - \sum_{i=0}^{k} \lambda_i (r - rc)^i \phi^{(i)}(r_c), \qquad (15)$$

with $\lambda_i \in [0, 1]$ and fixed $k \in \mathbb{N}_0$, and estimate T_c theoretically or via MC simulations for different values of λ_i.

5.2 Van der Waals Equation of State

We now consider the van der Waals equation of state with critical parameters

$$\left[(1 + \Delta p) + 3 \frac{1}{(\Delta v + 1)^2} \right] [3(\Delta v + 1) - 1] = 8(1 + \theta), \qquad (16)$$

with $\theta = \frac{T - T_c}{Tc}$, $\Delta p = \frac{p - p_c}{p_c}$, $\Delta v = \frac{v - v_c}{v_c}$, and molar volume v. The critical exponent of the Van der Waals corresponds to the mean-field universality class, whereas we have considered a 3D particle system corresponding to the $d = 3$ Ising universality class, where d is the dimension of the system. The behavior around the critical point is different for the two universality classes, e.g., for the order parameter, the behavior around the critical point is described by

$$\Delta v \propto (|T - T_c|)^{-\beta}, \qquad (17)$$

with values $\beta = 0.5$ for the mean-field universality class, and $\beta = 0.325$ for the 3D Ising universality class. Similarly, one can compare all other critical parameters of these universality classes.

6 Conclusion

We were able to estimate the critical temperature $T_C \approx 0.94$, and were able to fit the gas-liquid binodal using the scaling-law, with $\beta = 0.325$, and the coexistence width, given by the gas-liquid density average.

In our discussion, we compare our gas-liquid binodal with results from the literature that consider other interaction potentials. We also find a different behavior around the critical point compared to the mean-field universality class, where $\beta = 0.5$.

Several improvements can be made and will be discussed in Appendix C. The accuracy of the results remains to be determined, e.g., finite-size effects were not considered.

The program and all the simulation data can be found on GitHub [5].

A Scaled Utot

Let us consider the isotropic change of volume of a cubic simulation box, i.e., $V_{\text{old}} = l_{\text{old}}^3 \rightarrow V_{\text{new}} = l_{\text{new}}^3$. As mentioned in Subsection 3.3, we wish to avoid computing $U(\vec{R}_{\text{new}})$ from scratch during the simulation. The force-shifted Lennard-Jones potential (see Eq. (3)) can be written as

$$U(\vec{R}_{\text{old}}) = U_{12}(\vec{R}_{\text{old}}) - U_6(\vec{R}_{\text{old}}) - U_1(\vec{R}_{\text{old}}) - U_{r_c}, \quad (18)$$

with

$$U_{12}(r) = 4\epsilon \left(\frac{\sigma}{r}\right)^{12}, \qquad U_6(r) = 4\epsilon \left(\frac{\sigma}{r}\right)^{6},$$

$$U_1(r) = r \cdot \left(\left.\frac{\mathrm{d}\phi(r)}{\mathrm{d}r}\right|_{r=r_c}\right), \quad U_{r_c} = \phi(r_c) - r_c \left.\frac{\mathrm{d}\phi(r)}{\mathrm{d}r}\right|_{r=r_c}. \quad (19)$$

Note that we have left out the sum over all particle interactions (see Eq. (7)) for simplicity. The total potential energy of the new volume can easily be calculated after computing $U(\vec{R}_{\text{old}})$ numerically, as

$$U(\vec{R}_{\text{new}}) = \lambda^{12} U_{12}(\vec{R}_{\text{old}}) - \lambda^6 U_6(\vec{R}_{\text{old}}) - \lambda^{-1} U_1(\vec{R}_{\text{old}}) - U_{r_c}, \quad (20)$$

with the scaling factor $\lambda = l_{\text{old}}/l_{\text{new}}$, see Eq. (11). Note that the cutoff radius should not be rescaled, and so, U_{r_c} remains unchanged. The terms in Eq. (18) are stored individually during the simulation.

B Binodal Construction

The critical temperature of the binodal can be estimated via fit to the scaling law

$$\rho_L - \rho_G = B \left(1 - \frac{T}{T_c}\right)^{\beta}, \quad (21)$$

for $T < T_c$. The parameters B and T_c are chosen to best fit the binodal's simulation results. The exponent is set to $\beta = 0.325$, as for the 3D Ising universality class. Additionally, the coexistence diameter is drawn to get an estimate of the critical density ρ_c. The coexistence density line drawn in Fig. 6 is drawn by fitting the average liquid-gas density at every temperature, i.e., by fitting to $(\rho_G + \rho_L)/2$. The linear fit is given by

$$T_{\text{fit}} = T_0 - k \left(\frac{\rho_G + \rho_L}{2}\right), \quad (22)$$

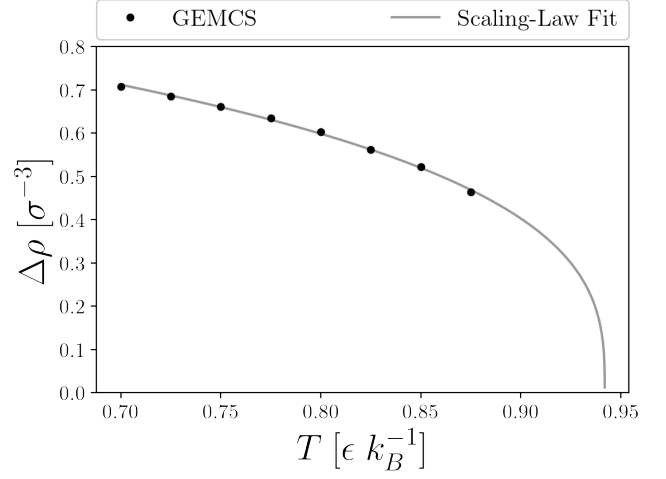with fit parameters $T_0 \approx 2.41$, and $k \approx 4.58$.

Figure 9: The numerical liquid-gas density difference $\Delta\rho = \rho_L - \rho_G$ (dots) is fitted to the scaling law (gray line), with fit parameters $B \approx 1.11$, and $T_c \approx 0.94$ (see Eq. (21)).

One can derive the binodal's density fit curves for the gas and liquid phase (as seen in Fig 6) from Eqs. (21) and (22):

$$\rho_{G,\text{fit}}(T) = -\frac{B}{2}\left(1 - \frac{T}{T_c}\right)^{\beta} - \frac{T - T_0}{k},$$

$$\rho_{L,\text{fit}}(T) = -\rho_{G,\text{fit}}(T) - 2\frac{T - T_0}{k}. \quad (23)$$

C Improvements

Several improvements could be made to the work presented in this report, regarding the GEMCS algorithm, the gathered numerical data, and simulation-error discussion.

The initial thermodynamical parameters of the GEMCS were chosen to be $N_\alpha = N/2$, $V_\alpha = V/2$, and T fixed, for both subsystems, i.e., for $\alpha = \mathrm{I}$ and $\alpha = \mathrm{II}$. However, one could in principle choose biased initial parameters N_α and V_α for faster convergence. The simulation's parameters $d_{\max}$, $dV_{\max}$ (see sections 3.1 and 3.3), P_d, P_n, and P_v (see Section 4.2), were chosen empirically after many simulation trials optimizing for fast convergence, and therefore, are not optimal. A parameter search can be made, optimizing for convergence time, to get better simulation parameters.

We have set a simulation-length limit of 10^5 MC sweeps for all temperatures, except for $T = 0.875$, where the simulation length was increased to approximately $2 \cdot 10^5$ MC sweeps. Increasing the length of the simulation may allow for more accurate simulation results. Moreover, we may also be able to observe phase separation for some temperatures $T > 0.875$ in longer simulations, as was the case for $T = 0.875$. Getting more data on temperatures $T > 0.875$ will yield a better estimate of the critical temperature T_c (see Fig. 9).

We have neglected the finite-size effects of the simulation in our discussion. Considering this, and possibly other effects, will provide a more accurate description of the gas-liquid binodal.

D   Large-Temperature Sampling

No phase separation was observed for large temperatures in the range $0.875 < T < T_c$. The MC simulation cannot sample effectively in this temperature range (see lower right subfigure of Fig. 10). The Phase separation could (in principle) be observed for some $T > 0.875$ given more simulation time. However, it is nearly impossible to sample close to T_c, because the phases become nearly identical.
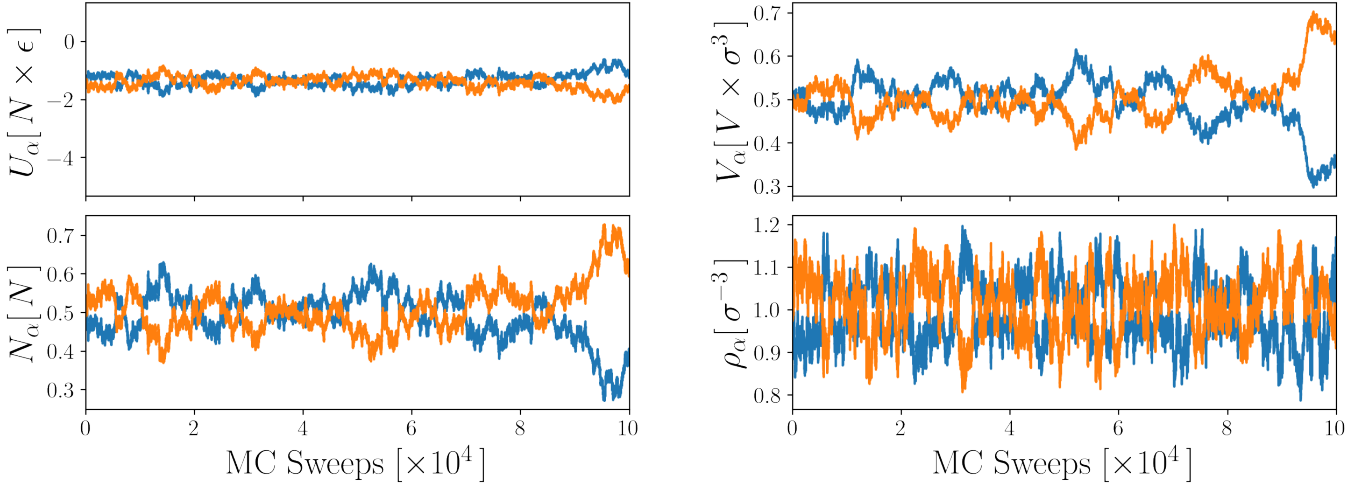

Figure 10: The subsystems, $\alpha = I$ (orange) and $\alpha = II$ (blue), are not able to equilibrate in the given simulation length of 10^5 MC sweeps for the temperature $T = 0.9$ (color online). No phase separation was observed by increasing the simulation length in this case. Similar results were observed for temperatures $0.875 < T < T_c$. As before, the evolution of each subsystem's potential energy U_α, volume V_α, particle number N_α, and particle density ρ_α are shown in the figure's upper left, upper right, lower left, and lower right corner respectively.

E   Simulations' Standard Deviation

The fluctuations around the equilibrium average increase in size over the temperature T, as shown by the increasing standard deviation of the Gaussian fit curves in Fig. 11. It is particularly noticeable for the lower densities, i.e., the gas phase, where the Gaussian fit is relatively sharp at $T = 0.7$ and significantly more spread out at $T = 0.875$.
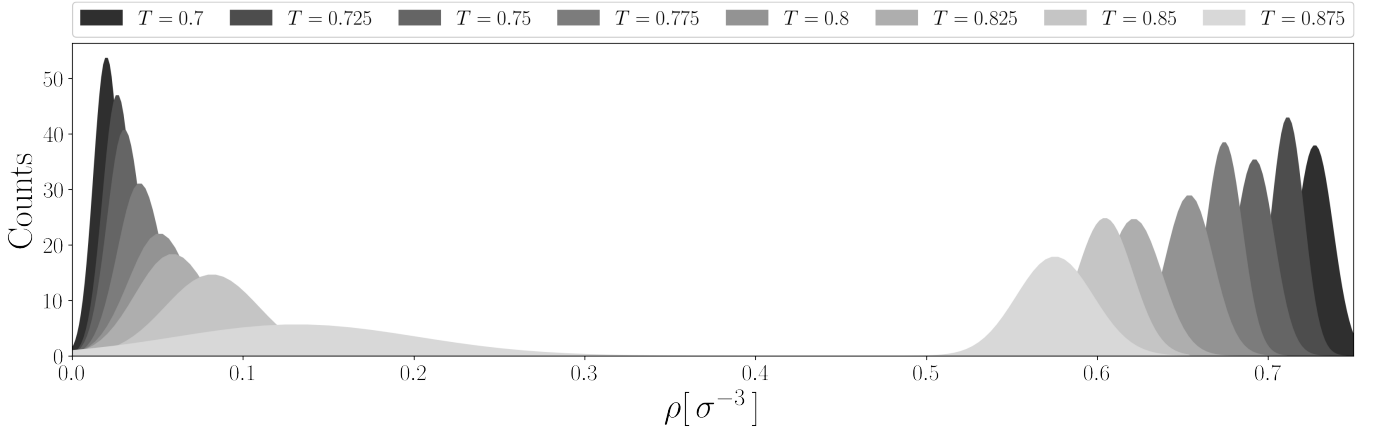

Figure 11: Gaussian fit curves plotted for the temperatures $T \in \{0.7, 0.725, 0.75, 0.775, 0.8, 0.825, 0.85, 0.875\}$. The standard deviation of the Gaussian curve increases over the temperature, particularly for the lower densities, i.e., for the gas phase. See Fig 5 for reference.

References

[1] J.-P. Hansen and L. Verlet, "Phase transitions of the lennard-jones system," *Phys. Rev.*, vol. 184, pp. 151–161, Aug 1969. `https://link.aps.org/doi/10.1103/PhysRev.184.151`.

[2] J. Vrabec, G. K. Kedia, G. Fuchs, and H. Hasse, "Comprehensive study of the vapour–liquid coexistence of the truncated and shifted lennard–jones fluid including planar and spherical interface properties," *Molecular Physics*, vol. 104, no. 9, pp. 1509–1527, 2006. `https://doi.org/10.1080/00268970600556774`.

[3] P. J. Horbach, "Lecture on computational physics," 2020.

[4] A. Rohatgi, "Web plot digitizer," 2021. `https://automeris.io/WebPlotDigitizer`.

[5] J. M. Henning, "Liquid-gas transition studied via gibbs ensemble monte carlo simulation," 2021. `https://github.com/jmsett/Liquid-Gas-Transition-Studied-via-GEMCS`.